Machine-learning energy-preserving nonlocal closures for turbulent fluid flows and inertial tracers

Alexis-Tzianni G. Charalampopoulos and Themistoklis P. Sapsis[*]
Department of Mechanical Engineering, Massachusetts Institute of Technology, Cambridge, Massachusetts 02139, USA

(Received 14 February 2021; accepted 4 January 2022; published 23 February 2022)

We formulate a data-driven, physics-constrained closure method for coarse-scale numerical simulations of turbulent fluid flows. Our approach involves a closure scheme that is nonlocal both in space and time, i.e., the closure terms are parametrized in terms of the spatial neighborhood of the resolved quantities but also their history. The data-driven scheme is complemented with a physical constraint expressing the energy conservation property of the nonlinear advection terms. We show that the adoption of this physical constraint not only increases the accuracy of the closure scheme but also improves the stability properties of the formulated coarse-scale model. We demonstrate the presented scheme in fluid flows consisting of an incompressible two-dimensional turbulent jet. Specifically, we first develop one-dimensional coarse-scale models describing the spatial profile of the jet. We then proceed to the computation of turbulent closures appropriate for two-dimensional coarse-scale models. Training data are obtained through high-fidelity direct numerical simulations. We also showcase how the developed scheme captures the coarse-scale features of the concentration fields associated with inertial tracers, such as bubbles and particles, carried by the flow but not following the flow. We thoroughly examine the generalizability properties of the trained closure models for different Reynolds numbers, as well as radically different jet profiles from the ones used in the training phase. We also examine the robustness of the derived closures with respect to the grid size. Overall, the adoption of the constraint results in an average improvement of 26% for one-dimensional closures and 29% for two-dimensional closures, being notably larger for flows that were not used for training.

DOI: 10.1103/PhysRevFluids.7.024305

I. INTRODUCTION

Turbulent fluid flows in nature and engineering are characterized by a wide range of spatial and temporal scales with nonlinear interactions making their reduced order modeling a challenging task. Over the last decades, several ideas have emerged that successfully model turbulent fluid flows, such as large eddy simulations [1,2]. However, these methods still require very high resolution to satisfactory model the large scale dynamics, as well as features associated with those. This is an important computational obstacle, especially for applications involving uncertainty quantification, optimization, and risk analysis, where there is a need for a large number of accurate simulations.

Recent machine-learning advances have sparked a new interest in utilizing deep neural networks to develop reduced order models for turbulent flows. The machine-learning closures abandon the path of a closed-form expression for the closure terms into utilizing experimental or costly high-fidelity computations to train a neural network and predict the nonlinear energy transfers

[*] Corresponding author: sapsis@mit.edu

between resolved and unresolved scales. One such effort of utilizing deep neural networks for turbulent flows appeared in Ref. [3], where nonlinear autoencoders were utilized to reconstruct the near wall field in a turbulent flow. Since then, there has been a plethora of efforts focusing on machine-learning closures using different data-driven schemes, such as artificial neural networks in fluid flows [4–7] and multiphase flows [8,9], random forest regressions [10], spatially nonlocal schemes such as convolutional neural networks [11], stochastic data-driven representations using generative adversarial networks [12], reinforcement learning [13], and with applications ranging from engineering turbulence to geophysics and beyond (see Ref. [14] for a recent review).

One of the great advantages of machine-learning closures is their capability to seamlessly model nonlocality in time. In this paper, a nonlocal but causal modeling of the closure terms implies that for the prediction of the closure terms at a particular time, only present and past information is used. Indeed, there is no *a priori* reason to expect that the closure terms of a complex system will behave in a Markovian manner, i.e., depend only on the current reduced-order state of the system. On the contrary, Takens embedding theorem [15] states that if we observe only a limited number of the state variables of a system, in principle, we can still obtain the attractor of the full system by using delay embedding of the observed state variables. Therefore, it is essential to incorporate memory effects when we model closure terms for turbulent fluid flows. This approach has found success in a number of physical applications involving bubble motion and multiphase flows [16,17], as well as the reduced-order modeling of chaotic dynamical systems [18–20].

On the other hand, machine-learning schemes allow us to parametrize the closure terms using a large number of input variables, opening the possibility for nonlocal models in space (see Ref. [11] for an application to the advection of a passive scalar). Spatially, nonlocal models have been advocated for turbulent closures and there is a plethora of related ideas ranging from scale-dependent closures [21], non-local Reynolds stress models [22], and fractional-operator closures [23]. Several ideas related to functional neural networks or operator neural networks have shown great promise in this direction [24,25] and have recently been of great interest in the context of turbulent closure models [26–28].

Beyond local closures, deep neural networks have also been used successfully in combination with the underlying governing equations for reconstructing complex fluid flows and identifying flow parameters. Specifically, physics-informed neural networks [29] identify the optimal solution (either the flow itself or parameters associated with it) by minimizing an objective function that contains Navier-Stokes equations, as well as scattered data in space and time. Inclusion of the governing equations significantly improves the behavior of the data-driven scheme, while the representation of the solution in terms of a neural network circumvents the need for a grid or spatial discritization scheme. The method has shown great promise for reconstructing fluid flows given spatiotemporal measurements [30], as well as recovering macroscopic quantities such as lift or drag for vortex-induced vibration problems [31]. Previous efforts along this line include the embedding of symmetries such as Galilean invariance to the neural net predictions for an anisotropic Reynolds stress tensor [32,33].

Our aim in this paper is to formulate energy-preserving spatiotemporally nonlocal turbulent closures which are *a priori* consistent with the conservation properties of the advection term in Navier-Stokes equations. Specifically, we utilize machine learning schemes which represent the effect of the small scales at each spatial location, using as input the large scale features of the flow in a spatial neighborhood of this location. Past values of the large scale features are also employed as inputs for the turbulent closures in a causal manner. These data-driven schemes are enforced to be consistent with physical constraints expressing the energy exchanges between resolved and unresolved scales. These constraints follow from the energy-conserving properties of the nonlinear advection operator in Navier-Stokes and have been utilized previously in the context of uncertainty quantification and stochastic closure models [34–37]. In contrast to previous efforts where the full system equation is used as a constraint, assuming perfect knowledge of the equation form and /or parameters (e.g., Ref. [30]), the formulated constraint in this paper expresses a universal property of the advection terms, i.e., that they do not create nor destroy kinetic energy of the flow. To improve the stability properties of the computed closures, we also employ imitation learning [38]. This method is then tested as a proof of concept in turbulent two-dimensional multiphase fluid flows, where an underlying incompressible carrier fluid advects inertial particles.

We first formulate the objective function used in the training phase. This step also includes the physical constraint and its derivation using Gauss theorem. We subsequently consider a forced two-dimensional jet flow. We first take into account the invariance of the flow in one direction to derive one-dimensional machine-learned closures using direct numerical simulation (DNS) information. As a next step, we apply the method on the computation of two-dimensional turbulent closures that do not rely on this special symmetry. We compare the obtained coarse-scale model with DNSs and assess its generalizability properties for different Reynolds numbers, as well as different jet profiles which have not been used in the training phase. We thoroughly examine the role of the physical constraint on the stability properties and accuracy of the coarse-scale equations. In addition, we assess our closure scheme on capturing the evolution of concentration for inertial tracers, such as bubbles and aerosols.

II. FORMULATION OF ENERGY-PRESERVING CLOSURE SCHEMES

Our aim is to derive Eulerian, data-driven closure schemes for turbulent fluid flows, as well as for inertial tracers advected by those. These closure schemes will not only rely on DNS training data but also on the physical constraint that follows from the energy conservation principles that the nonlinear advection terms satisfy [34,35]. The effectiveness of the closure schemes is assessed by how well the coarse-scale equations can reproduce the mean flow characteristics for problems that reach a statistical equilibrium. Higher order closures may be utilized to improve predictions for higher order statistics such as the flow spectrum. However, in this paper we will focus on closures that aim to model the mean flow characteristics.

First, we introduce a spatial-averaging operator that will define the coarse scale version of the quantities of interest and their evolution equations. Specifically, we decompose any field of interest f as

$$f = \overline{f} + f', \tag{1}$$

where $\overline{f}$ corresponds to the large-scale component of the quantity and f' corresponds to the small-scale component. As a result, we always have $\overline{f'} = 0$.

A. Averaged Navier-Stokes equations

We consider the Navier-Stokes equations in dimensionless form:

$$\frac{D\mathbf{u}}{Dt} = -\nabla p + \frac{1}{\mathrm{Re}}\Delta\mathbf{u} + \nu\nabla^{-4}\mathbf{u} + \mathbf{F}, \tag{2}$$

$$\nabla\cdot\mathbf{u} = 0, \tag{3}$$

where $\mathbf{u}$ is the velocity field of the fluid, p its pressure, Re is the Reynolds number of the flow, $\frac{D}{Dt}$ is the material derivative operator, and $\mathbf{F}$ denotes an external forcing term. Parameter ν is a hypoviscosity coefficient aiming to remove energy from large scales and maintain the flow in a turbulent regime. Using the decomposition Eq. (1) into the fluid flow Eq. (2) and applying the averaging operator, we obtain

$$\partial_t\overline{\mathbf{u}} = -\overline{\mathbf{u}}\cdot\nabla\overline{\mathbf{u}} - \overline{\mathbf{u}'\cdot\nabla\mathbf{u}'} - \nabla\overline{p} + \frac{1}{\mathrm{Re}}\Delta\overline{\mathbf{u}} + \nu\nabla^{-4}\overline{\mathbf{u}} + \overline{\mathbf{F}}, \tag{4}$$

$$\nabla\cdot\overline{\mathbf{u}} = 0. \tag{5}$$

Clearly, the averaged evolution equations do not comprise a closed system anymore due to the nonlinearity of the advection term. As a result, the term $\overline{\mathbf{u}' \cdot \nabla \mathbf{u}'}$ is not defined by the evolution equations and needs to be parametrized.

B. Averaged advection equation for inertial tracers

One can follow a similar process for the advection equation governing the motion of small inertial tracers. In particular, for small inertia particles their Lagrangian velocity, $\mathbf{v}$, is a small perturbation of the underlying fluid velocity field [39,40]:

$$\mathbf{v} = \mathbf{u} + \epsilon\left(\frac{3R}{2} - 1\right)\frac{D\mathbf{u}}{Dt} + O(\epsilon^2), \quad \epsilon = \frac{\mathrm{St}}{R} \ll 1, \quad R = \frac{2\rho_f}{\rho_f + 2\rho_p}, \tag{6}$$

where $\epsilon = \frac{\mathrm{St}}{R} \ll 1$ is a parameter representing the importance of inertial effects, St is the particle or bubble Stokes number, and $R = \frac{2\varrho_f}{\varrho_f + 2\varrho_p}$ is a density ratio with ϱ_p and ϱ_f being the density of the particle or bubble and the flow, respectively. Equation (6) arises from geometric singular perturbation theory in the limit of small particle inertia [39]. For this asymptotic limit, the presented manifold is always attracting trajectories exponentially fast [40]. However, errors due to the finite order truncation of the asymptotic expansion will result in inaccuracies for timescales larger than $O(\epsilon^{-2})$.

By introducing ρ as the concentration of tracers at a particular point, we can write the following transport equation:

$$\partial_t \rho + \nabla \cdot (\mathbf{v}\rho) = \nu_2 \Delta^4 \rho. \tag{7}$$

The right-hand-side of the transport equation represents a hyperviscosity term. Introducing the decomposition of Eq. (1) in the evolution Eqs. (6) and (7), we obtain

$$\overline{\mathbf{v}} = \overline{\mathbf{u}} + \epsilon\left(\frac{3R}{2} - 1\right)(\partial_t \overline{\mathbf{u}} + \overline{\mathbf{u}} \cdot \nabla \overline{\mathbf{u}} + \overline{\mathbf{u}' \cdot \nabla \mathbf{u}'}), \tag{8}$$

$$\partial_t \overline{\rho} + \nabla \cdot (\overline{\mathbf{v}}\overline{\rho}) + \overline{\nabla \cdot (\mathbf{v}'\rho')} = \nu_2 \Delta^4 \overline{\rho}. \tag{9}$$

Once again, the closure term $\overline{\nabla \cdot (\mathbf{v}'\rho')}$ appears, which requires parametrization. Note that the evolution equations of the carrier fluid [Eqs. (4) and (5)] and the transported inertial particles [Eqs. (8) and (9)] are both in dimensionless form.

C. Data-driven parametrization of the closure terms

While the full Navier-Stokes equations and the associated advection equations are Markovian and spatially local, i.e., the evolution of the flow or concentration field in a specific location and time instant depends only on the current time instant and the current neighborhood, this is not necessarily the case for the averaged version of these equations. In particular, for the averaged equations we typically do not have access to the full-state information required to fully describe the evolution of the system. In this case, the missing information is the small-scale dynamics.

To overcome this limitation, we recall Takens embedding theorem [15], which states that if we observe only a limited number of the state variables of a system, in principle, we can still obtain the attractor of the full system by using delay embeddings of the observed state variables. In other words, under appropriate conditions there is a map between the delays of the observed state variables and the full state system. Although the theorem itself is several decades old, we can now rely on recently developed data-driven schemes that can implement such mapping as part of their training process, enhancing the accuracy of predictions (see, e.g., Refs. [18,20]). To this end, we parametrize the closure terms with *nonlocal in time* (but still causal) representations, based on long-short-term memory (LSTM) recurrent neural networks (RNNs) and temporal convolutional networks (TCNs)

[41]. The specific RNN implementation was picked based on its tested ability to incorporate long-term memory effects of hundreds of time delays, while simpler RNN models suffer from vanishing or exploding gradients [42].

Beyond nonlocality in time, we also choose to employ nonlocality in space, that is, given a point in space $\mathbf{x}$, we use information from points that lie in a small neighborhood of $\mathbf{x}$. Clearly, incorporating information from the entirety of the domain is not only computationally infeasible but also redundant and can lead to stability issues. For this reason, we use convolutions in space to make sure that we incorporate information only from a region around each point and not from the entire domain. The parametrization is based on a stacked LSTM architecture [43], which utilizes LSTM layers with the detail that all input and recurrent transformations are convolutional.

As a result, the closure terms are modeled in the following form:

$$\overline{\mathbf{u}'\cdot\nabla\mathbf{u}'}(\mathbf{x},t)=\mathbb{D}_{\mathbf{u}}[\theta_1;\overline{\xi}[\alpha(\mathbf{x}),\,\chi(t)]],\qquad \overline{\nabla\cdot(\mathbf{v}'\rho')}(\mathbf{x},t)=\mathbb{D}_{\rho}[\theta_2;\overline{\zeta}[\alpha(\mathbf{x}),\,\chi(t)]],\tag{10}$$

where $\overline{\xi}$ and $\overline{\zeta}$ are (averaged) flow features to be selected, $\alpha(\mathbf{x})$ denotes a preselected neighborhood of points around $\mathbf{x}$ over which the averaged state is considered, i.e., $\alpha(\mathbf{x})=\{\mathbf{x},\mathbf{x}+\mathbf{x}_1,\mathbf{x}+\mathbf{x}_2,\ldots,\mathbf{x}+\mathbf{x}_N\}$, and $\chi(t)$ denotes the history of the averaged state backward from time t, i.e., $\chi(t)=\{t,t-\tau_1,\ldots,t-\tau_2,\ldots,t-\tau_N\}$. The vectors θ_1 and θ_2 denote the hyperparameters of the neural networks and their optimization is performed empirically. The spatial neighborhood, $\alpha(\mathbf{x})$, is selected such that if we further increase it, the training error does not significantly reduce anymore. Note however, that the number of points in space that have to be considered in $\alpha(\mathbf{x})$ is dependent on the discretization of the domain, i.e., if we increase the resolution of our model, the number of neighborhood points in $\alpha(\mathbf{x})$ should increase, respectively, so the input information used as input in the closure always corresponds to the same spatial neighborhood. In the numerical study that follows, we study the effect of spatial discretization. We use a similar approach for the temporal history, $\chi(t)$.

1. Temporal integration

We point out that our numerical goal is inline prediction. This means that the neural nets described by Eqs. (10) must be coupled with the evolution Eqs. (4)–(9). For a simple forward Euler scheme for temporal integration, this would imply that by knowing the values of $\overline{\mathbf{u}}$, $\overline{\rho}$ at time t, we can predict the closure terms at time t using Eqs. (10) and use their values to integrate Eqs. (4)–(9) by one time step δt, so we compute $\overline{u}_1$, $\overline{\rho}$ at time $t+\delta t$. However, if we want to use a higher-order integration scheme like a fourth-order explicit Runge-Kutta, we need to evaluate the closure terms at time $t+\delta t/2$ as well. Since we do not have access to the required time history for such a prediction, we instead integrate in time not by δt but by $2\delta t$ and thus get a time-integration error for $O[(2\delta t)^4]$.

D. Physical constraints

An important feature of our data-driven closure schemes is the requirement to satisfy certain physical principles. Specifically, we utilize the energy flux constraint that the advection term does not alter the total kinetic energy of the model [35,36]. This constraint, follows from Gauss identity. Specifically, for any scalar field, ψ, β, and divergence-free field, Φ, we have from Gauss identity,

$$\int_\Omega \frac{\partial\psi}{\partial x_j}\beta\Phi_j d\mathbf{x}=-\int_\Omega\frac{\partial\beta}{\partial x_j}\psi\Phi_j d\mathbf{x}+\int_{\partial\Omega}\psi\beta\Phi_j n_j d\mathbf{x},\tag{11}$$

where n_j is the unit vector on the boundary, $\partial\Omega$. Applying the above for $\psi=\beta=u_k$ and $\Phi_j=u_j$, we obtain the general three-dimensional constraint:

$$\int_\Omega \mathbf{u}\cdot(\mathbf{u}\cdot\nabla)\mathbf{u}d\mathbf{x}=\int_{\partial\Omega}\mathcal{E}\,\mathbf{u}\cdot\mathbf{n}\,d\mathbf{x},\quad \mathcal{E}=\frac{1}{2}\mathbf{u}\cdot\mathbf{u},\tag{12}$$

where Ω is the domain in which the fluid flow is defined. The above constraint essentially expresses the fact that the nonlinear advection terms do not change the total kinetic energy of the system. In what follows, we will consider the case of periodic boundary conditions, where the right-hand side in Eq. (12) vanishes. However, the same ideas are applicable for arbitrary boundary conditions. We apply the decomposition Eq. (1) and the spatial averaging operator to this equation and obtain

$$\begin{aligned}\int_\Omega \bar{\mathbf{u}}\cdot(\bar{\mathbf{u}}\cdot\nabla)\bar{\mathbf{u}}d\mathbf{x} + \int_\Omega \bar{\mathbf{u}}\cdot\overline{(\mathbf{u}'\cdot\nabla)\mathbf{u}'}d\mathbf{x} + \int_\Omega \overline{\mathbf{u}'\cdot(\bar{\mathbf{u}}\cdot\nabla)\mathbf{u}'}d\mathbf{x}\\ + \int_\Omega \overline{\mathbf{u}'\cdot(\mathbf{u}'\cdot\nabla)\bar{\mathbf{u}}}d\mathbf{x} + \int_\Omega \overline{\mathbf{u}'\cdot(\mathbf{u}'\cdot\nabla)\mathbf{u}'}d\mathbf{x} = 0.\end{aligned} \tag{13}$$

From the last equation, we have the *physical constraint* that the closure term $\mathbb{D}_{\mathbf{u}}$ must satisfy

$$\begin{aligned}\int_\Omega \bar{\mathbf{u}}\cdot\mathbb{D}_{\mathbf{u}}[\theta_1;\bar{\xi}[\alpha(\mathbf{x}),\chi(t)]]d\mathbf{x} = A[\mathbf{u}] \triangleq -\int_\Omega \bar{\mathbf{u}}\cdot(\bar{\mathbf{u}}\cdot\nabla)\bar{\mathbf{u}}d\mathbf{x} - \int_\Omega \overline{\mathbf{u}'\cdot(\bar{\mathbf{u}}\cdot\nabla)\mathbf{u}'}d\mathbf{x}\\ - \int_\Omega \overline{\mathbf{u}'\cdot(\mathbf{u}'\cdot\nabla)\bar{\mathbf{u}}}d\mathbf{x} - \int_\Omega \overline{\mathbf{u}'\cdot(\mathbf{u}'\cdot\nabla)\mathbf{u}'}d\mathbf{x},\end{aligned} \tag{14}$$

where $A[\mathbf{u}]$ is a function that depends on the training data and the discretization. Such a constraint can be added to the training process in a straightforward manner through the objective function. We emphasize that one could formulate a physical constraint based, e.g., on the Navier-Stokes equations directly. However, this assumes exact knowledge of the flow specifics. This is not the case here since the above constraint expresses a universal property, i.e., that advection terms do not create nor destroy energy.

E. Objective function for training

In terms of the training process itself, we normalize the input and output data as usually suggested (see, e.g., Ref. [44]). The loss function for this problem is chosen to be the single-step prediction mean-square error superimposed with the physical constraint. This can be formulated as

$$L(\theta_1) = \int_{\Omega\times T} ||\mathbb{D}_{\mathbf{u}}[\theta_1;\bar{\xi}] - \overline{(\mathbf{u}'\cdot\nabla)\mathbf{u}'}||^2 d\mathbf{x}dt + \lambda\int_T \left|\int_\Omega \bar{\mathbf{u}}\cdot\mathbb{D}_{\mathbf{u}}[\theta_1;\bar{\xi}]d\mathbf{x} - A[\mathbf{u}]\right|dt, \tag{15}$$

where λ is a hyperparameter which is chosen so the two terms of the loss function are of the same order of magnitude. More specifically, $\lambda = \lambda^* = 10^1$. It also reported that if $\lambda = \lambda^*/10$ is chosen, then the results are almost identical to the case where the constraint is not used. Furthermore, if $\lambda = 10\lambda^*$, then the generated closure is unstable both for unimodal and bimodal jets. On the other hand, for the advection equation, we have the objective function:

$$L(\theta_2) = \int_{\Omega\times T} ||\mathbb{D}_\rho[\theta_2;\bar{\zeta}[\alpha(\mathbf{x}),\chi(t)]] - \nabla\cdot(\overline{\mathbf{v}'\rho'})||^2 d\mathbf{x}dt. \tag{16}$$

Note that a similar constraint with the one in Eq. (15) can be formulated for the mass conservation property of the tracers. However, this approach is not pursued here. An important question is which flow features are important as input for each of the two models. We examine this issue in detail in the following sections.

F. Imitation learning

While the single-step prediction error is used for training, the aim of this paper aims to use these models for multistep prediction. Any such predictor introduces errors and these compounding errors change the input distribution for future prediction steps, breaking the train-test independent and identically distributed assumption that is common in supervised learning. Under these circumstances, the error can be shown to grow exponentially [45]. This effect was observed in the current setup as well, with the averaged equations becoming unstable. To alleviate this problem, a version of the imitation learning presented in Ref. [45], the Data as Demonstrator (DaD) method, is used. It is also noted that since in the current setup, the evolution equation of the carrier fluid is independent of the evolution of the transported particles, the process can only be showcased for the carrier fluid closure. This process is shown in an algorithmic manner in Algorithm 1.

Expanding on what Algorithm 1 presents, the algorithm first computes the reference flow features $\overline{\mu}^{\mathrm{Ref}}$ and reference closure term values $\mathbb{D}_{\mathbf{u}}^{\mathrm{Ref}}$ from DNSs. Then, the neural network for the carrier fluid closure-term $\mathbb{D}_{\mathbf{u}}^{\mathrm{Ref}}$ is trained. For the next step, define a fixed number of time steps M_T and an error tolerance δ_1. The goal of this stage is, for all time instances that are included in the training set as the fluid flow is evolved for M_T time steps forward in time, the L^2-error at the final time step is smaller than δ_1. This condition has to be satisfied for all flows that are included in the training set. If this condition is satisfied, the closure is assumed to be stable and thus the training process is rendered complete. If not, for each initial training point, mark as M_s the time step forward in time at which the condition was first violated. The imitation algorithm requires that an artificial data point $[\overline{\mu}^*|_{t=t+M_s}, \mathbb{D}_{\mathbf{u}}^*(t+M_s)]$ is created, which corresponds to the value of the closure term that is required, so the flow features return to their appropriate reference value $\mu^{\mathrm{DNS}}(t+M_s+1)$ at the M_s+1 time step forward. These data points are not physical solutions of some DNS solver. They artificially introduce stability to the closure scheme so as to allow the model to return close to the training data when it deviates. This extra amount of data is introduced to the previous set of training data and steps 1 and 2 of Algorithm 1 are repeated.

This process is repeated until the closure is stable and displays good predictive accuracy in all training cases. A more rigorous display of this condition is seen in Algorithm 1. For the present setup, this was achieved after 20 iterations. The same process is followed for the closure scheme of the transported particles, $\mathbb{D}_\rho = \overline{\boldsymbol{\nabla} \cdot (\mathbf{v}'\rho')}$. Note that noise, in the form of some artificial colored or white noise, is not added to the training data. However, the use of the DaD algorithm increases the training size by generating new training data that have noise as a result of the error in the predictions of the neural network as it is propagated as the flow evolves.

III. FLUID FLOW SETUP

For the validation and assessment of the formulated closures, we consider a two-dimensional turbulent jet where bubbles are also advected as passive inertial tracers. Specifically, the velocity field governing the bubbles is different from that of the underlying fluid flow (due to inertia effects), but the bubbles do not affect in any way the underlying fluid flow.

Algorithm 1. Training of closure scheme.

```
   Input: Reference closure terms $\{\mathbb{D}_i^{\mathrm{DNS}}(t_0), ..., \mathbb{D}_i^{\mathrm{DNS}}(t_p)\}$ $i = \mathbf{u}, \rho$, computed from DNS
   Data: Neural Network architecture, averaging-operator, discretization, $\delta t$ and input flow features $\overline{\mu}$
   Result: Predicted closure terms $\{\mathbb{D}_i^{\mathrm{ML}}(t_0), ..., \mathbb{D}_i^{\mathrm{ML}}(t_p)\}$ $i = \mathbf{u}, \rho$.
 1 Set $\overline{\mu}^{\mathrm{Ref}} = \overline{\mu}^{\mathrm{DNS}}$ and $\mathbb{D}_{\mathbf{u}}^{\mathrm{Ref}} = \mathbb{D}_{\mathbf{u}}^{\mathrm{DNS}}$;
 2 Train $\mathbb{D}_{\mathbf{u}}^{\mathrm{ML}}$ using $\mathbb{D}_{\mathbf{u}}^{\mathrm{Ref}}$;
 3 for $i = 1, ..., 20$ do
 4     for $t = 0, \delta t, ..., T\delta t$ do
 5         $s \to t$;
 6         while $\left\|\mathbb{D}_{\boldsymbol{u}}^{ML}(s) - \mathbb{D}_{\boldsymbol{u}}^{DNS}(s)\right\| > \delta_1$ do
 7             Predict $\overline{\mathbf{u}}^{\mathrm{ML}}(s + \delta t)$;
 8             Predict $\mathbb{D}_{\mathbf{u}}^{\mathrm{ML}}(s + \delta t)$;
 9             $s \to s + \delta t$;
10         end
11         Compute $\mathbb{D}_{\mathbf{u}}^*(s)$ so that $\overline{\mathbf{u}}^{\mathrm{ML}}(s + \delta t) = \overline{\mathbf{u}}^{\mathrm{DNS}}(s + \delta t)$;
12         Set $(\overline{\mu}^{\mathrm{Ref}}, \mathbb{D}_{\mathbf{u}}^{\mathrm{Ref}}) = (\overline{\mu}^{\mathrm{DNS}}, \mathbb{D}_{\mathbf{u}}^{\mathrm{ML}}) \cup (\overline{\mu}^*|_s, \mathbb{D}_{\mathbf{u}}^*(s))$;
13     end
14     Train $\mathbb{D}_{\mathbf{u}}^{\mathrm{ML}}$ using $\mathbb{D}_{\mathbf{u}}^{\mathrm{Ref}}$;
15 end
```

We set up a turbulent jet that fluctuates around a steady-state jet solution, $\mathbf{u}_{\text{jet}}$. In its dimensionless form, this system of equations can be written as

$$\frac{D\mathbf{u}}{Dt} = -\nabla p + \frac{1}{\text{Re}}\Delta\mathbf{u} + \nu\nabla^{-4}(\mathbf{u} - \mathbf{u}_{\text{jet}}) + \mathbf{F}, \tag{17}$$

$$\nabla \cdot \mathbf{u} = 0, \tag{18}$$

where $\mathbf{u} = (u_1, u_2)$ and $\text{Re} = O(10^3)$. The domain is assumed rectangular, doubly periodic, i.e., $\mathbf{x} = (x, y) \in S^2 = [0, 2\pi] \times [0, 2\pi]$. For initial conditions, since we desire anisotropy in our flow, we use Gaussian jet structures of the general form

$$u_{1,\text{jet}} = \sum_i A_i \exp[-c_i(y - \beta_i)^2], \quad u_{2,\text{jet}} = 0, \tag{19}$$

where A_i, c_i, β_i are parameters. The role of the external forcing term, $\mathbf{F}$, is twofold: (i) it contains a large-scale component to maintain the jet structure by balancing the dissipation term and (ii) it has a small-scale and small-amplitude component to perturb the flow and trigger instabilities so we enter a turbulent regime. To achieve turbulence, we choose a forcing term that acts only on a specific waveband with $6 \leqslant \|\mathbf{k}\| \leqslant 7$. Exciting a flow with a forcing localized only in a narrow wave-number interval is common practice in turbulence literature [46–49].

Therefore, we adopt a form $\mathbf{F} = -\frac{1}{R}\Delta u_{\text{jet}} + f$, with f being

$$f(\mathbf{x}, t) = \sum_i A_i(t)\cos(\mathbf{k}\cdot\mathbf{x} + \omega_i), \tag{20}$$

where $6 \leqslant |\mathbf{k}| \leqslant 7$, $A_i(t)$ are random vectors that follow a Gaussian white noise distribution (each one independent from the other) and ω_i are phases sampled from a uniform distribution over $[0, 2\pi]$. The standard deviation for these amplitudes is set to 0.03. This ensures that the energy and enstrophy inputs are localized in Fourier space and only a limited range of scales around the forcing is affected by the details of the forcing statistics. Furthermore, such a forcing ensures that the system reaches a jetlike statistical steady state after a transient phase. Due to the small-scale forcing being essentially homogeneous in space, we can deduce that the statistical steady-state profile is only dependent on y (since our large-scale forcing and initial conditions depend only on y). We solve this flow using a spectral method and 256^2 modes.

For the bubbles, we use the perturbed advection field [Eqs. (6)] and the corresponding advection Eq. (7). For the simulations presented, we use the inertial parameters, $\epsilon = 0.05$ and $R = 2$, which correspond to small bubbles. A typical snapshot of the described flow can be seen in Fig. 1. During training, unimodal jets of different Reynolds numbers are used with parameter values $A_1 = 1, c_1 = 2, \beta_1 = \pi$. Furthermore, for testing purposes, bimodal jets are considered with the Reynolds numbers varying and parameters $A_1 = 1, \beta_1 = 0.8\pi, c_1 = 3$ and $A_2 = 1, \beta_2 = 1.2\pi, c_2 = 3$.

IV. TRAINING OF THE CLOSURES

We study the effectiveness of the proposed closure scheme in two different setups. In the first setup, we take advantage of the translational invariance of the flow in the x direction. This allows us to obtain a closed averaged equation for the y profile of the jet. In the second case, we do not rely on this symmetry and obtain closures directly for the two-dimensional flow. We will compare the adopted architectures for both the case of utilizing the energy constraint presented above and not.

A. One-dimensional closures for the jet profile

We take advantage of the translational invariance of the flow in the x direction and select the spatial-averaging operator to be integration along the full x direction and local spatial averaging

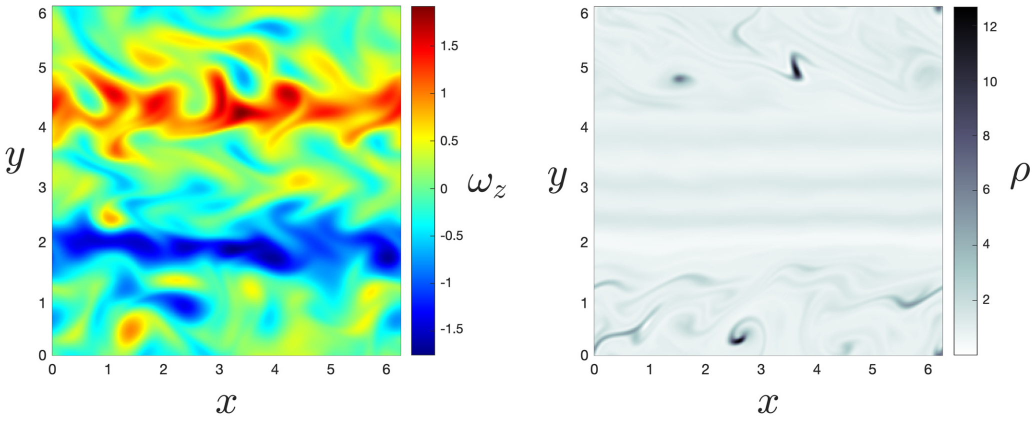

FIG. 1. Snapshot of vorticity (left) and bubble density field (right) for a bimodal turbulent jet for Re $=$ 1000, and bubble parameters $\epsilon = 0.05$ and $R = 2$.

along the y direction,

$$\bar{f}(y) = \frac{1}{2\pi} \iint_{S^2} w_l(y' - y) f(x, y') dx dy', \tag{21}$$

where $w_l(y' - y) = \frac{1}{2l}[H(y' - y - l) - H(y' - y + l)]$ is the piecewise constant averaging window of length $2l$; here $l = \frac{2\pi}{20}$. Applying the averaging operator to the governing equations, we obtain the equation for the y profile of the jet. Note that based on our averaging operator for this case, we have $\bar{u}_2 = 0$ and $\bar{u}_1$ is only a function of y. To this end, we have

$$\partial_t \bar{u}_1 = -\mathbb{D}_{u_1} + \frac{1}{\mathrm{Re}} \partial_y^2 \bar{u}_1 + \nu \nabla^{-4}(\bar{u}_1 - u_{1,\mathrm{jet}}) + \overline{F}_1, \tag{22}$$

$$\partial_t \overline{\rho} + \partial_y(\overline{v_2}\ \overline{\rho}) + \mathbb{D}_\rho = \nu_2 \partial_y^4 \overline{\rho}. \tag{23}$$

Therefore, the objective function used for training of the flow closure takes the form

$$L(\theta_1) = \int_{\Omega \times T} ||\mathbb{D}_{u_1}[\theta_1; \overline{\xi}] - \overline{(\mathbf{u}' \cdot \nabla)\mathbf{u}'}||^2 d\mathbf{x} dt + \lambda \int_T \left| \int_\Omega \bar{u}_1 \cdot \mathbb{D}_{u_1}[\theta_1; \overline{\xi}] d\mathbf{x} - A[\mathbf{u}] \right| dt, \tag{24}$$

where $A[\mathbf{u}] = -\int_\Omega \overline{\mathbf{u}' \cdot (\mathbf{u}' \cdot \nabla)\mathbf{u}'} d\mathbf{x}$. On the other hand, the objective function for the density field closure takes the form

$$L(\theta_2) = \int_{\Omega \times T} ||\mathbb{D}_\rho[\theta_2; \overline{\zeta}[\alpha(\mathbf{x}), \chi(t)]] - \nabla \cdot (\overline{\mathbf{v}'\rho'})||^2 d\mathbf{x} dt. \tag{25}$$

The neighborhood $\alpha(y)$ is selected to have five nodes in total,

$$\alpha(y) = \{y + m\delta y\}, \quad \delta y = 2\pi/80, \quad m = -2, -1, ..., 2,$$

while the temporal horizon in the past is selected as

$$\chi(t) = \{t - m\delta\tau\}, \quad \delta\tau = 10^{-2}, \quad m = 1, 2, ..., 12.$$

Both the spatial extent of the neighborhood and the memory are chosen as the threshold values above which any further increase does not result in a significant difference in the training and validation errors.

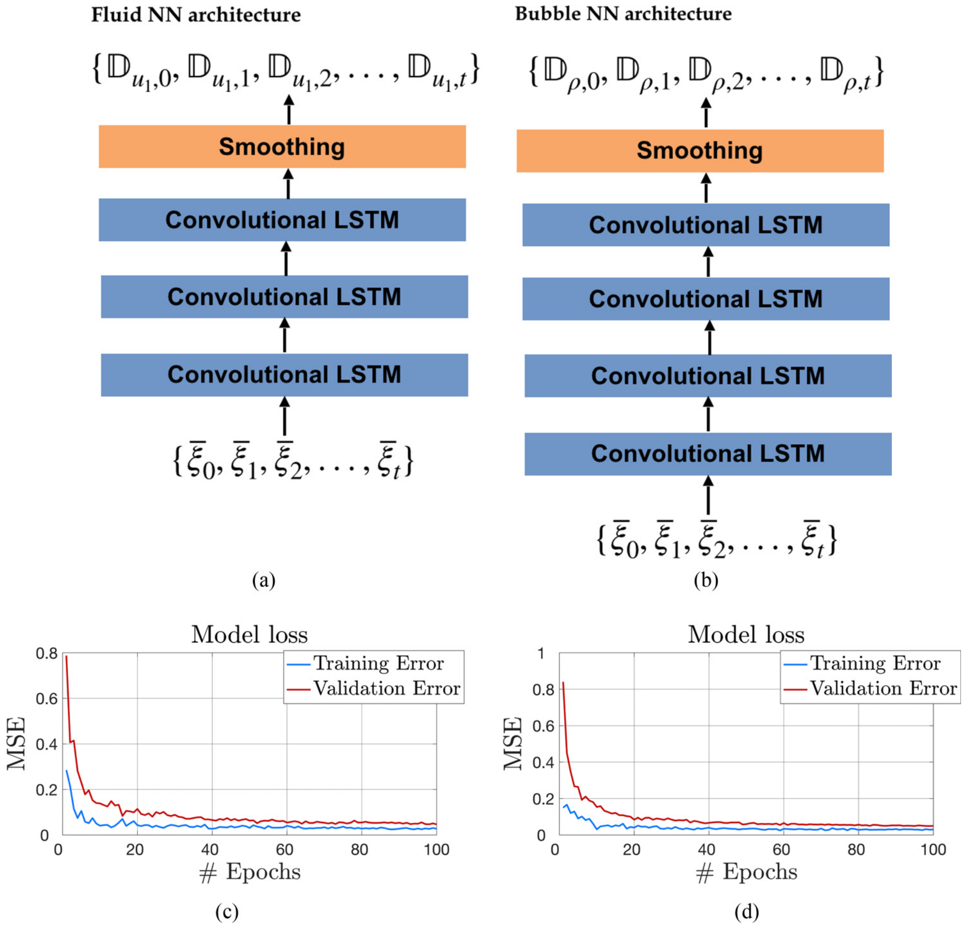
Fluid NN architecture
$\{\mathbb{D}_{u_1,0}, \mathbb{D}_{u_1,1}, \mathbb{D}_{u_1,2}, \dots, \mathbb{D}_{u_1,t}\}$
Smoothing
Convolutional LSTM
Convolutional LSTM
Convolutional LSTM
$\{\overline{\xi}_0, \overline{\xi}_1, \overline{\xi}_2, \dots, \overline{\xi}_t\}$
Bubble NN architecture
$\{\mathbb{D}_{\rho,0}, \mathbb{D}_{\rho,1}, \mathbb{D}_{\rho,2}, \dots, \mathbb{D}_{\rho,t}\}$
Smoothing
Convolutional LSTM
Convolutional LSTM
Convolutional LSTM
Convolutional LSTM
$\{\overline{\xi}_0, \overline{\xi}_1, \overline{\xi}_2, \dots, \overline{\xi}_t\}$
Model loss
MSE
0.8
0.6
0.4
0.2
0
0
20
40
60
80
100
# Epochs
Training Error
Validation Error
Model loss
MSE
1
0.8
0.6
0.4
0.2
0
0
20
40
60
80
100
# Epochs
Training Error
Validation Error

(a)

(b)

(c)

(d)

FIG. 2. (a) Architecture of the LSTM neural network for parametrizing the term $\mathbb{D}_t = \partial_y(\overline{u_1'u_2'})$. (b) Architecture of the LSTM neural network for parametrizing the term $\mathbb{D}_t = \partial_y(\overline{v_2'\rho'})$. (c) Mean-square training-error (solid line) and validation error (dashed line) for $\mathbb{D}_u$. (d) Mean-square training-error (solid line) and validation error (dashed line) for $\mathbb{D}_\rho$.

1. Neural network architecture

We assess two different architectures for our closure scheme. In the first case, we represent the flow closure with three convolutional-LSTM layers and the density closure with four convolutional-LSTM layers (16 time delays). Further increase of the number of layers does not offer any significant improvement in the training and validation errors. The adopted architectures are presented in Figs. 2(a) and 2(b). For the second machine learning architecture, we use four-layer temporal convolutions to model the memory terms of our closure for both the flow and the density fields. The architecture in this case is depicted in Figs. 3(a) and 3(b). An important difference between the two architectures that is worth emphasizing is associated with their computational cost. Specifically, in the LSTM architecture, we have a memory term that is updated at each time step and, to this end, LSTM needs to only operate on the flow features at each time step. On the other hand, TCN layers operate on the entire included time history, making them more computationally expensive.

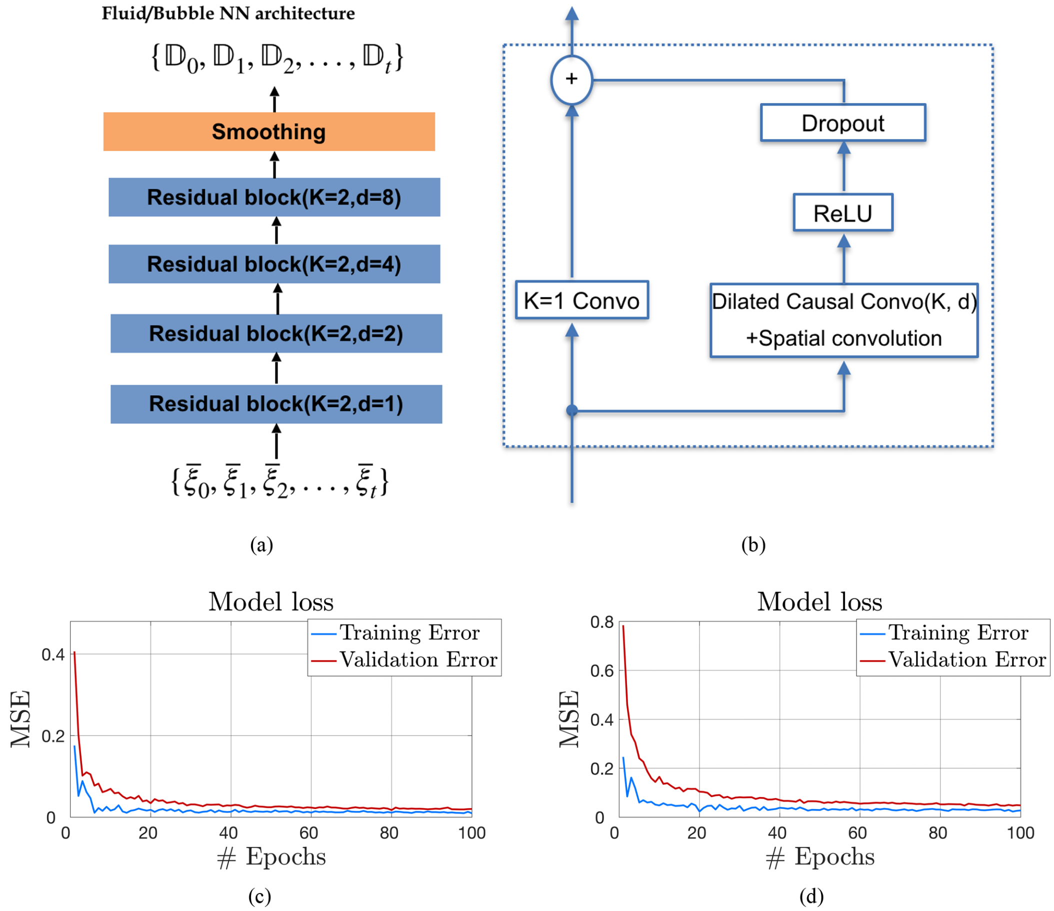

(a)

(b)

(c)

(d)

FIG. 3. (a) Architecture of the TCN neural network for parametrizing the terms $\partial_y(\overline{u_1'u_2'})$ and $\partial_y(\overline{v_2'\rho'})$. (b) Inner architecture of a residual block. (d) Mean-square training error (solid line) and validation error (dashed line) for $\mathbb{D}_u$. (e) Mean-square training error (solid line) and validation error (dashed line) for $\mathbb{D}_\rho$.

2. *Feature selection*

The selection of the flow features that are used as inputs for the data-driven closures is done numerically by testing different combinations of basic flow features. We eventually choose the combination that minimizes the training and the validation error. It is important to emphasize that if we rely only on the training error, we run the risk of overfitting. We carry out this process individually for each of the closure terms for the Navier-Stokes equation and the transport equation.

For the closure term $\mathbb{D}_{\mathbf{u}}$, we select as possible flow features the quantities $\overline{u}_1$, $\partial_t\overline{u}_1$, $\partial_y(\overline{u_1'u_2'})$. All input flow features are separately normalized to have variance equal to 1. Table I summarizes the performance for different combinations over 100 periods for the TCN and LSTM architectures with the physical constraint. It is observed that while $\{\partial_t\overline{u}_1, \partial_y(\overline{u_1'u_2'})\}$ drastically decreases the training error, the inclusion of the mean flow profile $\overline{u}_1$ strongly improves the validation error. Since the best validation error is achieved in this case, all considered flow features are employed.

For the implementation of the presented closure scheme, the input features are not imposed to be Galilean invariant. Requiring the input features to be Galilean invariant can be justified when the closure scheme is intended to model drastically different flows (different boundary conditions, flow geometry, or significantly different Reynolds numbers). Machine learning universal closures

TABLE I. Feature selection for the one-dimensional closure of Navier-Stokes

		ξ feature selection			
		cTCN		cLSTM	
Features	Dimesions	Train-MSE	Val-MSE	Train-MSE	Val-MSE
$\overline{u}_1$	1	0.094	1.712	0.102	1.501
$\partial_t\overline{u}_1$	1	0.037	0.535	0.041	0.501
$\partial_y(\overline{u'_1u'_2})$	1	0.028	0.144	0.033	0.139
$\overline{u}_1$, $\partial_t\overline{u}_1$	2	0.042	0.418	0.056	0.511
$\overline{u}_1$, $\partial_y(\overline{u'_1u'_2})$	2	0.023	0.159	0.028	0.157
$\partial_t\overline{u}_1$, $\partial_y(\overline{u'_1u'_2})$	2	0.021	0.092	0.026	0.085
$\overline{u}_1$, $\partial_t\overline{u}_1$, $\partial_y(\overline{u'_1u'_2})$	3	0.021	0.029	0.025	0.032

for turbulence are beyond the scope of this effort. This is because this task is associated with extreme obstacles, such as selection of training data which are representative of essentially every possible dynamical regime and geometry, and the assumption that there is a machine learning architecture that can generalize well over such a vast range of conditions. Instead, the goal here is to develop closures that can generalize well over a family of flows with common topology and dynamics. To this end, the need for the features to be Galilean is not necessary, since the frame of reference for all produced jet flows is the same and the magnitude of the examined jets is very similar.

For the closure of the transport equation, we carry out the same process in Table II, where we present the training and validation error over 100 periods. We observe that the single most important feature is $\overline{\rho}$. Based on the mean-square error (both training and validation), we choose the combination of $\overline{u}$, $\overline{\rho}$, $\partial_t\overline{u}$, $\partial_y(\overline{\rho'v'})$. In Fig. 2, we present the values of both validation and training errors with respect to the number of epochs. These are quite similar, hinting toward generalizability of the predictions. It is worth mentioning that when spatial derivatives are added to the selected feature sets shown previously, training and validation error didn't improve. This could be a result of nonlocal information of the (averaged) fluid flow profile and density profile used as input, allowing the convolutions to combine these values in a finite-difference sense to derive spatial derivative information that is needed. However, in the case of trying to test this model to drastically different flow setups, the Galilean invariant partial spatial derivatives are probably appropriate to replace the non-Galilean averaged features, i.e., the fluid flow profile and density profile.

TABLE II. Feature selection for closure of bubble transport equation.

		ζ feature selection			
		cTCN		cLSTM	
Features	Dimensions	Train-MSE	Val-MSE	Train-MSE	Val-MSE
$\overline{\rho}$	1	0.109	0.150	0.123	0.171
$\overline{\boldsymbol{v}}$	2	0.603	0.673	0.592	0.625
$\overline{\boldsymbol{v}}$, $\overline{\rho}$	3	0.081	0.090	0.094	0.101
$\overline{\boldsymbol{v}}$, $\overline{\rho}$, $\partial_t\overline{\boldsymbol{v}}$, $\partial_t\overline{\rho}$	6	0.058	0.060	0.061	0.064
$\overline{\boldsymbol{v}}$, $\overline{\rho}$, $\partial_t\overline{\boldsymbol{v}}$, $\partial_y(\overline{\rho'v'_2})$	6	0.028	0.039	0.042	0.088
$\overline{\boldsymbol{v}}$, $\overline{\rho}$, $\partial_t\overline{\rho}$, $\partial_y(\overline{\rho'v'_2})$	5	0.027	0.036	0.035	0.049
$\overline{\boldsymbol{v}}$, $\overline{\rho}.\partial_t\overline{\boldsymbol{v}}$, $\partial_t\overline{\rho}$, $\partial_y(\overline{\rho'v'_2})$	7	0.025	0.031	0.033	0.044

TABLE III. Feature selection for closure of Navier-Stokes.

		ξ feature selection			
		cTCN		cLSTM	
Features	Dimensions	Train-MSE	Val-MSE	Train-MSE	Val-MSE
$\bar{\boldsymbol{u}} = (\overline{u_1}, \overline{u_2})$	2	0.235	0.521	0.258	0.572
$\partial_t\bar{\boldsymbol{u}} = (\partial_t\overline{u_1}, \partial_t\overline{u_2})$	2	0.098	0.480	0.112	0.388
$\mathbb{D}_{\mathbf{u}}$	2	0.081	0.094	0.092	0.114
$\bar{\boldsymbol{u}}, \partial_t\bar{\boldsymbol{u}}$	4	0.069	0.485	0.100	0.522
$\bar{\boldsymbol{u}}, \mathbb{D}_{\mathbf{u}}$	4	0.048	0.082	0.067	0.094
$\partial_t\bar{\boldsymbol{u}}, \mathbb{D}_{\mathbf{u}}$	4	0.027	0.048	0.034	0.063
$\bar{\boldsymbol{u}}, \partial_t\bar{\boldsymbol{u}}, \mathbb{D}_{\mathbf{u}}$	6	0.020	0.039	0.027	0.055

B. Two-dimensional closures

In this case, our averaging operator was chosen to be local in both dimensions, x and y,

$$\bar{f}(x, y) = \frac{1}{2\pi} \iint_{S^2} w_{l_x}(y' - y) w_{l_y}(y' - y) f(x, y') dx dy', \tag{26}$$

where $l_x = l_y = \frac{2\pi}{12}$ are the averaging windows in the x and y directions, respectively. As objective functions, we used Eqs. (15) and (16). The spatial and temporal neighborhoods used in the closures are chosen as

$$\alpha(\mathbf{y}) = \{\mathbf{y} + m_1\delta\mathbf{x} + m_2\delta\mathbf{y}\}, \quad \delta x = 2\pi/48, \quad \delta y = 2\pi/48 \quad \text{and} \quad m_1, m_2 = -2, -1, ..., 2,$$
$$\chi(t) = \{t - m\delta\tau\}, \quad \delta\tau = 1/100, \quad m = 1, 2, ..., 12.$$

Similarly, with the one-dimensional closures, these numbers are based on the fact that further increase did not result in a significant difference in the training and validation errors. We employ the same neural network architectures that we used in the previous section.

1. Feature selection

For the closure term $\mathbb{D}_{\mathbf{u}}$ (corresponding to the fluid flow), we try as possible flow features the quantities $\bar{\boldsymbol{u}}$, $\partial_t\bar{\boldsymbol{u}}$, $\mathbb{D}_{\mathbf{u}}$. Results are shown for the case where the constraint is adopted (cTCN and cLSTM) in Table III in terms of training and validation errors. In this case, we observe that the single most important feature is the history of the Reynolds stresses. Furthermore, we see that the optimal combination consists of all the examined features.

For the closure of the transport equation, we carry out the same process in Table IV. We observe that the single most important features seems to be $\overline{\rho}$, similar to the one-dimensional case. For the results that follow, we choose the combination $\overline{\mathbf{v}}$, $\overline{\rho}$, $\partial_t\overline{\mathbf{v}}$, $\partial_t\overline{\rho}$, $\mathbb{D}_\rho$, which results in the minimum validation and testing errors.

V. VALIDATION AND GENERALIZABILITY FOR ONE-DIMENSIONAL CLOSURES

To showcase the generalizability properties of the obtained closures, we train on unimodal jets and test on bimodal ones. We mention again that the averaged model is one-dimensional and we use 80 points in space to simulate it. We compare the results of the averaged model with the predictions of the two-dimensional reference solutions that we computed using a spectral method and 256^2 modes. Each training case contains data in the time interval $T = [200, 600]$.

TABLE IV. Feature selection for closure of bubble transport equation.

		ζ feature selection			
		cTCN		cLSTM	
Features	Dimensions	Train-MSE	Val-MSE	Train-MSE	Val-MSE
$\overline{\rho}$	1	0.199	0.398	0.228	0.451
$\overline{\boldsymbol{v}} = (\overline{v_1}, \overline{v_2})$	2	0.320	0.591	0.318	0.515
$\overline{\boldsymbol{v}}, \overline{\rho}$	3	0.141	0.386	0.162	0.404
$\overline{\boldsymbol{v}}, \overline{\rho}, \partial_t \overline{\boldsymbol{v}}$	5	0.085	0.176	0.087	0.192
$\overline{\boldsymbol{v}}, \overline{\rho}, \partial_t \overline{\rho}, \mathbb{D}_\rho$	5	0.051	0.091	0.061	0.125
$\overline{\boldsymbol{v}}, \partial_t \overline{\rho}, \partial_t \overline{\boldsymbol{v}}, \mathbb{D}_\rho$	6	0.030	0.049	0.038	0.068
$\overline{\boldsymbol{v}}, \overline{\rho}, \partial_t \overline{\rho}, \partial_t \overline{\boldsymbol{v}}, \mathbb{D}_\rho$	7	0.016	0.032	0.031	0.047

A. Validation on unimodal jets

As seen in Sec. III, the unperturbed jet profile is chosen as

$$u_{1,\text{jet}} = \exp[-2(y-\pi)^2], \quad u_{2,\text{jet}} = 0. \tag{27}$$

We train four different models on unimodal jets of Re ∈ {650, 750, 850}. We use LSTM and TCN architectures with and without enforcing the physical constraint of Eq. (24). In Fig. 4, we present the time- and y-averaged mean-square error between the x-averaged profile of the DNS, $\bar{u}^*$ and the coarse scale model, $\bar{u}$:

$$||\bar{u}^* - \bar{u}||_2^2 = \frac{1}{2\pi T}\int_0^{2\pi}\int_{t_0}^{t_0+T}(\bar{u}^*(y,t) - \bar{u}(y,t))^2 dydt. \tag{28}$$

We observe that the TCN models clearly outperform the LSTM based closures. Moreover, training using the objective function that includes the physical constraint [Eq. (24)] for the advective terms (cTCN and cLSTM) significantly improves the testing results for the two architectures by 23% and 25%, respectively (Table V). This improvement comes at no additional cost in terms of data, but only using the physical constraint associated with the advection terms, which does not depend on the knowledge of any physical quantity of the flow or any other system-specific information.

In Fig. 5, we present additional results for the cTCN model (best performer). We showcase results both for the time-averaged profile for the fluid velocity and for the bubble distribution for

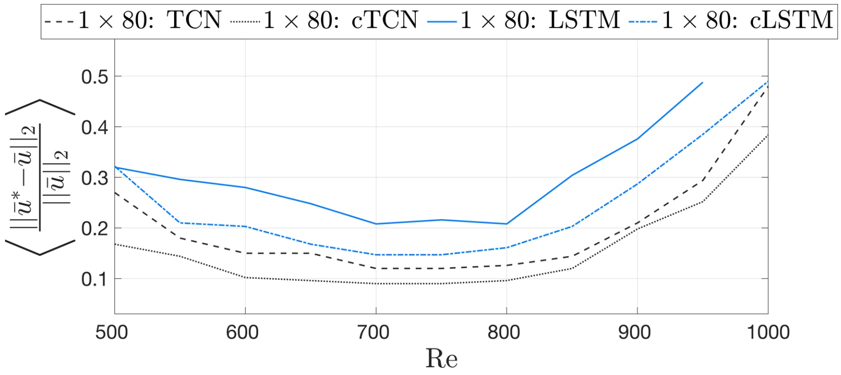

FIG. 4. Normalized error Eq. (28) for one-dimensional closure models using TCN, LSTM, and their constrained versions, cTCN and cLSTM, for unimodal jets. Training data includes unimodal jets with Re ∈ {650, 750, 850}.

TABLE V. Error decrease (Reynolds averaged) due to the physical constraint for one-dimensional closure schemes.

Architecture	Jet type	Error decrease
TCN-1D	Unimodal	23%
LSTM-1D	Unimodal	25%
TCN-1D	Bimodal	29%
LSTM-1D	Bimodal	27%

$\mathrm{Re} = 1000$. Comparisons are made between the time-averaged results that the one-dimensional closure scheme produces and the time- and x-averaged results of the two-dimensional reference solution. Specifically, the time-averaged jet profile is computed as

$$\langle \overline{\boldsymbol{u}}_1 \rangle (y) = \frac{1}{T} \int_{t_0}^{t_0+T} \overline{\boldsymbol{u}}_1(y, t) dt, \tag{29}$$

where $\bar{u}_1$ is the x-averaged reference solution and the temporal averaging parameters are chosen as $t_0 = 200$ and $T = 400$; note that we omit the first transient part of the simulation.

The results appear to be in very good agreement, showcasing that our closure scheme is able to predict the statistical steady state of the flow. We can also observe the Rayleigh instability that the initial jet profile (dashed line) undergoes due to the excitation by the external forcing. We note that the slight asymmetry that the velocity profile exhibits is due to a minor inhomogeneity of the forcing term along the y direction. We apply the same operation described above to compute $\langle \overline{\rho} \rangle$ from both the reference solution and the data-based closure scheme [Fig. 5(b)]. Again, we obtain very good agreement between the machine-learning approach and the reference solution, which has a nontrivial form, as the bubbles seem to cluster around the core of the jet and be repelled from the adjacent areas of the jet core.

B. Testing generalizability on bimodal jets

Next we test the generalizability of the closure schemes presented in the previous section on bimodal jets. Once again, we state that we train on unimodal jets (as described previously) while we test our scheme on bimodal jets with the unperturbed jet-structure of the fluid flow chosen (as seen in Sec. III) as

$$u_1 = \exp[-3(y - 0.8\pi)^2] + \exp[-3(y - 1.2\pi)^2], \quad \mathrm{Re} \in [500, 1000]. \tag{30}$$

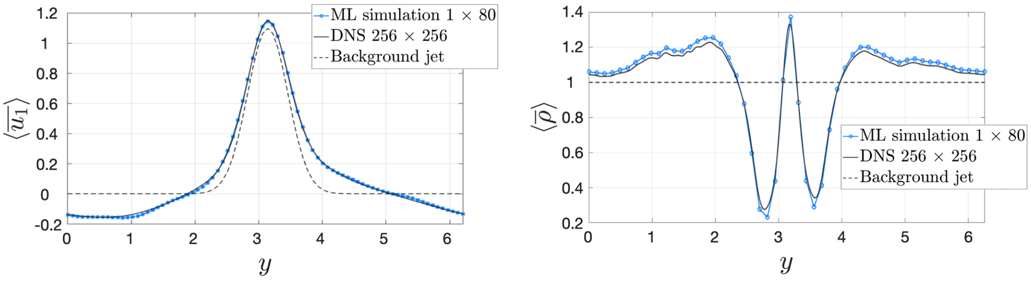

(a)

(b)

FIG. 5. Time-averaged profile of $\overline{\boldsymbol{u}}_1$ (left) and $\bar{\rho}$ (right) for the one-dimensional cTCN closure model (blue line) and the DNS (black line). The shape of the jet that is imposed by the large-scale forcing is depicted with dashed line. The simulation corresponds to $\mathrm{Re} = 1000$ while training included $\mathrm{Re} \in \{650, 750, 850\}$.

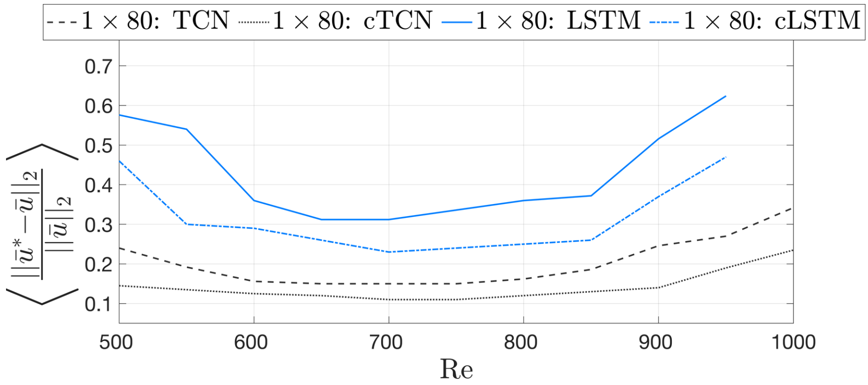

FIG. 6. Normalized error Eq. (28) for one-dimensional closure models error for one-dimensional closures applied on bimodal jets. Training data includes unimodal jets with Re = {650, 750, 850}.

In Fig. 6, we present the normalized mean-square error Eq. (28) between the reference solution and the one predicted by the closure model. As we can see, employing the physical constraint during training significantly improves the results. Specifically, we note that the errors of the cTCN and cLSTM remain at the same levels observed in the unimodal jet case (i.e., we have good generalizability properties in different flows), while the unconstrained version has significantly worse performance compared with the unimodal jet case. In addition, we observe much better behavior of the constrained closures when we move to Reynolds numbers higher than the ones used for training. In fact, for sufficiently large Reynolds the schemes based on the unconstrained closures become unstable.

Results regarding the time-averaged jet profile of $\bar{\boldsymbol{u}}_1$ and ρ are depicted in Fig. 7 for the cTCN architecture, where we can observe excellent agreement of the predicted profile with DNSs. We also apply the closure scheme on the transport Eq. (7) to compute the distribution of bubbles. We present the comparison of the mean distribution of bubbles between the cTCN closure model and DNS in Fig. 7(b). We note that the error for this case is slightly more pronounced compared with the one observed for the mean flow velocity in Fig. 7(a). This can be attributed to two factors: (i) the predictions of the transport model rely on the predictions of the coarse-scale model for the velocity field (hence error accumulates) and (ii) the closure model for the bubbles relies only on data since the energy-preserving constraint is not relevant.

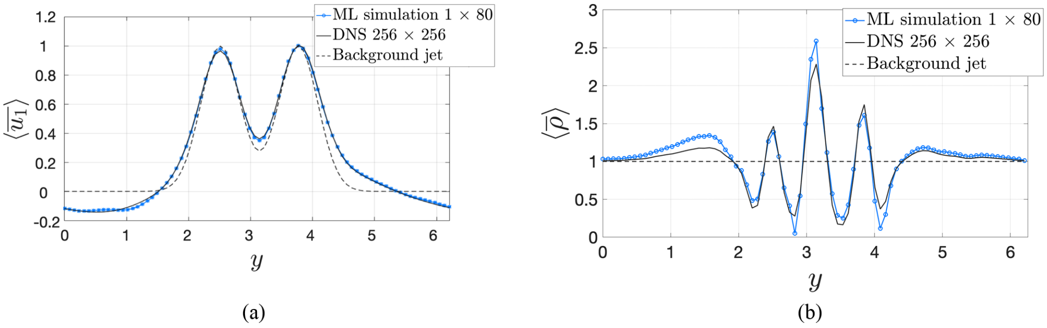

FIG. 7. Time-averaged profile of $\bar{\boldsymbol{u}}_1$ and $\bar{\rho}$ for the one-dimensional cTCN closure model (blue line) and the DNS (black line). The simulation corresponds to Re = 1000 and a bimodel background jet, while training data for the closures correspond to unimodal jets with Re ∈ {650, 750, 850}. The shape of the jet that is imposed by the large-scale forcing is depicted with dashed line.

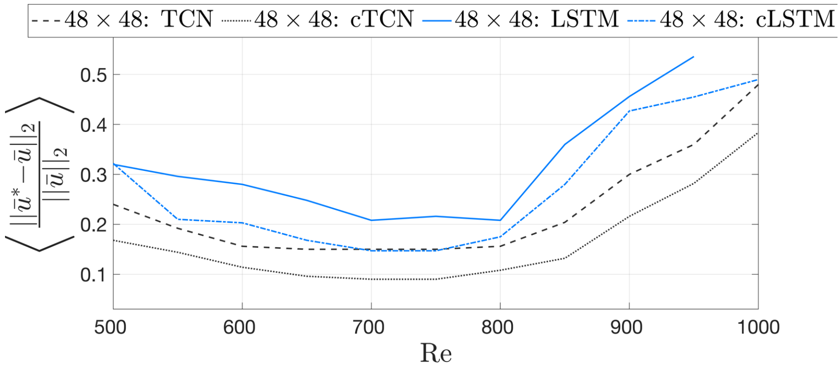

FIG. 8. Normalized mean-square error Eq. (31) of each two-dimensional closure model using TCN, LSTM, and their constrained versions for unimodal jets. Training includes data for unimodal jets with Re ∈ {650, 750, 850}.

A summary of the error improvement in the one-dimensional predictions due to the adoption of the physical constraint is presented in Table V. We present the improvement of the mean-square error for the mean flow, averaged over different Reynolds numbers. For all cases, this percentage ranges between 23% and 29% with the improvement being more pronounced for the bimodal setups, i.e., the setup that was not used for training.

VI. VALIDATION AND GENERALIZABILITY FOR TWO-DIMENSIONAL CLOSURES

Here we aim to showcase the application of our method on two-dimensional coarse-scale closures. As previously, we consider two cases: (i) we train on *unimodal* jets for flows with Reynolds number Re ∈ {650, 750, 850} and test on *unimodal* jets in the range Re ∈ [500, 1000] and not included in the training set and (ii) we once again train on *unimodal* jets (same Reynolds as before) and test on *bimodal* jets in the same Reynolds range as in case (i). For the coarse-scale model, we employ a resolution of 48 × 48, complemented with the ML-closure terms. We compare the energy spectra at the statistical steady state of the flows between the coarse-scale predictions and the two-dimensional reference solutions, i.e., for $t \in [200, 600]$.

A. Testing on a unimodal jet

In Fig. 8, we present the space-time-averaged mean-square error between the $x - y$ locally averaged DNS flow field [using Eq. (26)], $\bar{u}^*$, and the coarse scale model, $\bar{u}$:

$$||\bar{u}^* - \bar{u}||_2^2 = \frac{1}{(2\pi)^2 T} \int_0^{2\pi} \int_0^{2\pi} \int_{t_0}^{t_0+T} (\bar{u}^*(x, y, t) - \bar{u}(x, y, t))^2 dxdydt. \tag{31}$$

The results are in full consistency with the one-dimensional closures, i.e., cTCN has the best performance. We also present a detailed comparison for Re = 800 between the coarse model and the DNS in terms of the energy spectrum and mean profile the flow (Fig. 9). The energy spectrum is computed by obtaining the spatial Fourier transform at each time instant and then considering the variance of each Fourier coefficient over time. We plot the energy spectrum in terms of the absolute wave-number values. For both the flow field and bubble field, the coarse- model is able to accurately capture the mean profiles as well as the large scale features of the spectrum.

B. Testing generalizability on bimodal jets

We proceed to test the generalizability of the two-dimensional closure schemes on bimodal jets. The setup is identical with the one adopted for one-dimensional closures. In Fig. 10, we compare

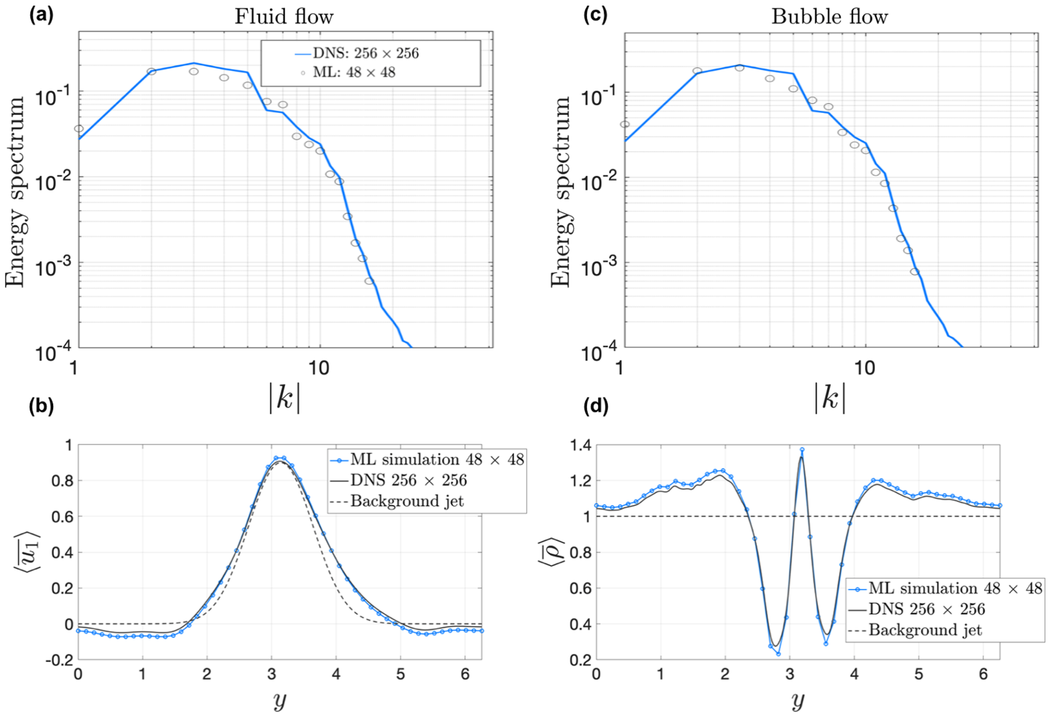

FIG. 9. Comparison of energy spectra and mean profiles for the flow velocity field [(a), (c)] and the bubble velocity field [(b), (d)] for unimodal jets. Blue lines correspond to DNSs on a 256 × 256 grid and the black circles correspond to the coarse model using two-dimensional closures (cTCN) on a 48 × 48 grid for Re = 800.

the normalized mean-square error between the locally averaged DNS solution and the one obtained form the coarse model. Consistent with previous results, the cTCN has the best performance. It is interesting to note that the performance is even better in the Reynolds regime outside the training data, i.e., for Re > 850.

The energy spectrum of the fluid velocity and the bubble velocity field as well as the corresponding mean profiles are compared with DNSs for Re = 800 in Fig. 11. In this case, we note that while there is good agreement between the mean profiles, there is some discrepancy between

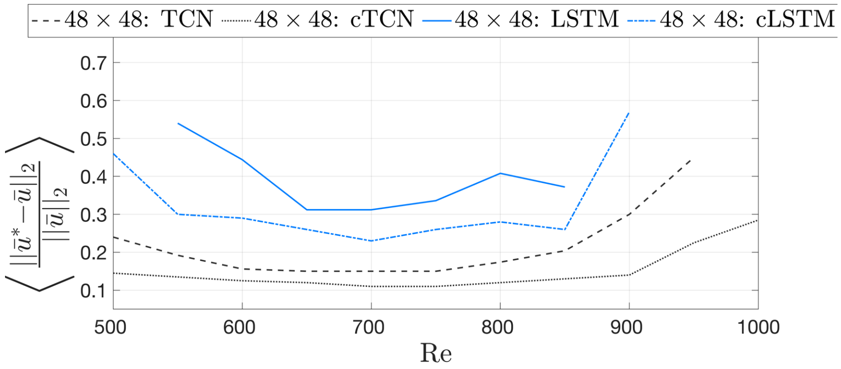

FIG. 10. Normalized mean-square error Eq. (31) for two-dimensional coarse models applied on bimodal jet flows. Training used data from unimodal flows with Re = {650, 750, 850}.

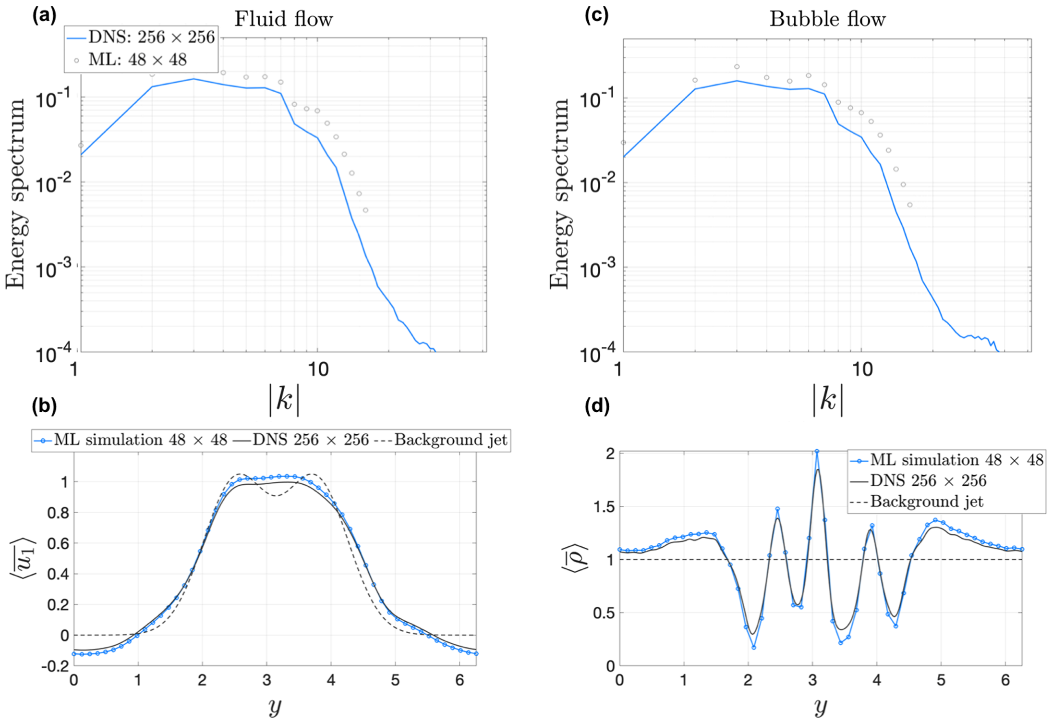

FIG. 11. Comparison of energy spectra and mean profiles for the fluid velocity field [(a), (c)] and the bubble velocity field [(b), (d)] for the case of a bimodal jet with Re = 800. Blue lines correspond to DNSs on a 256 × 256 grid and the black circles correspond to a coarse-model with two-dimensional cTCN closures on a 48 × 48 grid.

the approximate and exact spectra. To understand better the source of this discrepancy, we plot the energy spectrum of the flow in the k_x, k_y space (Fig. 12). As can be seen, the coarse model overestimates the spread of the energy of the fluctuations only in the x direction, which is consistent with the fact that the mean y profile of the flow is accurately modeled. This is not surprising given that the developed closures in this paper are designed to capture well the mean flow characteristics and not necessarily the energy spectrum. A closure approach based on second-order statistical equations (see, e.g., Ref. [36]) is beyond the scope of this paper and will be considered elsewhere.

The overall improvement in the two-dimensional predictions due to the adoption of the physical constraint is summarized in Table VI, where we show the improvement of the mean-square error for the mean flow, averaged over different Reynolds numbers. We note that for the TCN architecture, the improvement is more pronounced, close to 30%, and it is also robust for the case of a bimodal jet.

TABLE VI. Error decrease (Reynolds averaged) due to the physical constraint for two-dimensional closure schemes.

Architecture	Jet type	Error decrease
TCN-2D	Unimodal	30%
LSTM-2D	Unimodal	20%
TCN-2D	Bimodal	33%
LSTM-2D	Bimodal	31%

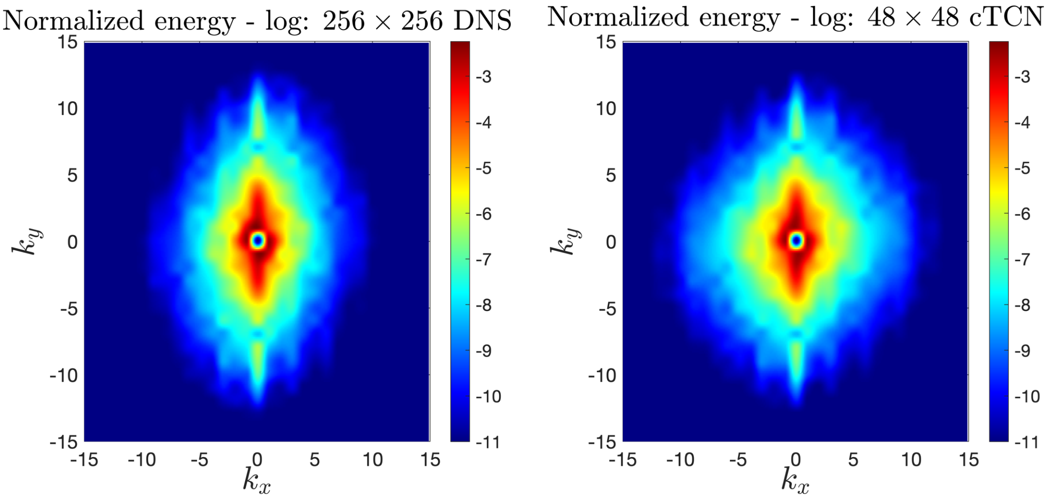

FIG. 12. Energy spectrum of the fluid flow for the bimodal jet for Re = 800. Comparison between the DNS (left) and the coarse-model based on 2D cTCN closures (right).

A quick comparison with the error-decrease values in Table V shows the L^2-error improvement is slightly better in the 1D (zonally averaged) coarse-scale model than in the 2D coarse-scale model. This result could be attributed to the fact that a 1D model will be less turbulent compared to a 2D coarse-scale simulation due to zonally averaging the flow and thus essentially neglecting perturbations along the x axis, making the simulations more stable.

C. Dependence on the coarse-model grid size

Finally, we showcase a numerical investigation for the relationship between the chosen grid size for the coarse-scale simulations and the mean-square error of the velocity of the fluid flow. For all results presented below, training data was chosen as previously (unimodal jets) and results are presented for bimodal jets. In Fig. 13(a), we vary the size of a $N_x \times N_y$ grid with $N_x = N_y \in \{16, 24, 32, 40, 48, 64, 80, 96\}$. We notice that there is significant improvement in our predictions as we refine the grid up to a grid size of 64 × 64 where the error saturates.

Since the variation of the mean profile of the flow is only along the y direction, having a coarser resolution along the less significant x direction should not hinder the predictions. To validate this property, we maintain a constant discretization in the x direction and vary the grid size only in the

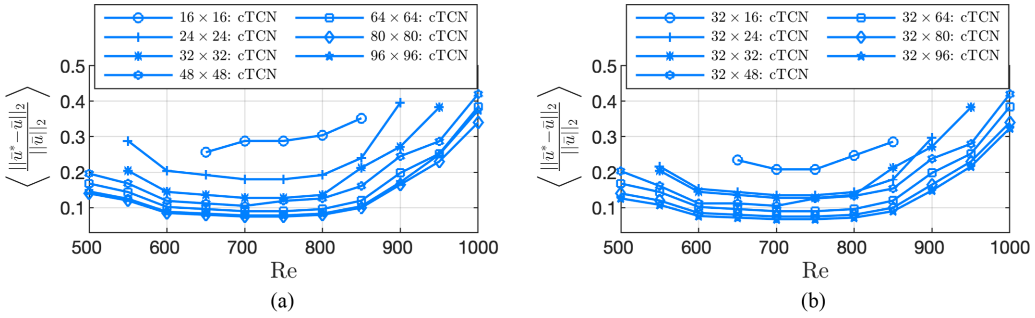

(a)

(b)

FIG. 13. Root-mean-square error for different grid-sizes using two-dimensional cTCN closures on bimodal jet.

y direction. Results are demonstrated in Fig. 13(b), showing clearly that by having a fine resolution only in the y direction is sufficient to achieve comparable performance with the fine resolution case in both directions: $N_x = N_y = 96$.

D. Limitations

While the proposed method adequately predicts flows that are distinct from those of the training set, it is important to state that the computed closure is not expected to be as effective in every fluid flow. This is due to the fact that, depending on the specifics of a fluid flow, such as dimensionality, boundary conditions, domain geometry, excitation terms, and the presence of additional dynamics such as Coriolis terms, the nonlinear interactions between scales are different. Therefore, aiming to machine learn universal closures that will work for every case is beyond the scope of this paper. Instead, our approach is to employ data from flows that have some common features with the flow we are interested in modeling, and combine this data with a universal constraint, the energy conservation by the nonlinear terms, to increase the accuracy of the computed closures. The optimal choice of input features is also expected to vary depending on the specifics of the flow and therefore a numerical examination of different combinations should be performed to achieve the most effective closure.

VII. CONCLUSIONS

We have demonstrated the application of the energy conservation property of the advection terms on machine-learning nonlocal closures for turbulent fluxes. We have adopted two neural network architectures, based on LSTM and TCN, to further include memory effects in our analysis. Clearly, the physical constraint is not restricted to these two frameworks and can be employed in other machine-learning architectures, as well as other fluid systems (e.g., environmental flows). We demonstrated the computed closures in two-dimensional jets in an unstable regime and showed that closures obtained from unimodal jets can be used for different jet geometries. The adoption of the physical constraint significantly and consistently improved the accuracy of the mean-flow predictions obtained from the corresponding coarse-scale models independently of the adopted architecture or the flow setup. This improvement was on average 26% for one-dimensional closures and 29% for two-dimensional closures, being notably larger for flows that were not used for training. Moreover, the constraint improved the numerical stability of the coarse-scale models, especially in Reynolds numbers, which were higher than the ones included in the training data sets. While the adopted examples are relatively simple, yet unstable, fluid flows, the presented energy constraints do not depend on the complexity of the flow. They are applicable for more complicated setups including boundary flows and transition phenomena–directions that we plan to pursue in the future.

ACKNOWLEDGMENTS

This paper has been supported through ONR-MURI Grant No. N00014-17-1-2676 and AFOSR-MURI Grant No. FA9550- 21-1-0058.

APPENDIX: COMPARISON OF A LOCAL CLOSURE-SCHEME APPROACH WITH NONLOCAL CLOSURE SCHEMES

To showcase the numerical benefits of using spatiotemporally nonlocal closure, it is first stated that when using a local closure in tandem with the constraint, the L^2 prediction error for a unimodal jet of $\mathrm{Re} = 800$ is 0.49. Furthermore, the computational cost to evolve the system by one time step is 3×10^{-3} [s], run on a single core of an Intel i9 2.3 GHz processor. In Table VII, prediction improvement and computational cost increases compared to the local closure scheme are presented for closures that are only nonlocal in time, only nonlocal in space, and finally spatiotemporally nonlocal.

TABLE VII. Error improvement and increase of computational cost with respect to a local closure scheme for a unimodal jet of Re = 800.

Architecture	Error decrease	Inline cost increase	Training cost increase
Spatially nonlocal closure	11%	285%	665%
Temporally nonlocal one-layer LSTM	30%	120%	365%
Temporally nonlocal three-layer LSTM	35%	250%	410%
Temporally nonlocal two-layer TCN	21%	380%	620%
Temporally nonlocal four-layer TCN	43%	610%	1100%
Spatiotemporally nonlocal one-layer LSTM	51%	700%	1830%
Spatiotemporally nonlocal three-layer LSTM	56%	1100%	3180%
Spatiotemporally nonlocal two-layer TCN	50%	950%	3410%
Spatiotemporally nonlocal four-layer TCN	80%	2820%	6840%

[1] P. Moin, K. Squires, W. Cabot, and S. Lee, A dynamic subgrid-scale model for compressible turbulence and scalar transport, Phys. Fluids A **3**, 2746 (1991).

[2] P. Sagaut and Y.-T. Lee, Large eddy simulation for incompressible flows: An introduction. Scientific computation series, Appl. Mech. Rev. **55**, B115 (2002).

[3] M. Milano and P. Koumoutsakos, Neural network modeling for near wall turbulent flow, J. Comput. Phys. **182**, 1 (2002).

[4] M. Gamahara and Y. Hattori, Searching for turbulence models by artificial neural network, Phys. Rev. Fluids **2**, 054604 (2017).

[5] R. Maulik, O. San, A. Rasheed, and P. Vedula, Subgrid modelling for two-dimensional turbulence using neural networks, J. Fluid Mech. **858**, 122 (2019).

[6] A. P. Singh, S. Medida, and K. Duraisamy, Machine-learning-augmented predictive modeling of turbulent separated flows over airfoils, AIAA J. **55**, 2215 (2017).

[7] X. I. A. Yang, S. Zafar, J.-X. Wang, and H. Xiao, Predictive large-eddy-simulation wall modeling via physics-informed neural networks, Phys. Rev. Fluids **4**, 034602 (2019).

[8] M. Ma, J. Lu, and G. Tryggvason, Using statistical learning to close two-fluid multiphase flow equations for a simple bubbly system, Phys. Fluids **27**, 092101 (2015).

[9] M. Ma, J. Lu, and G. Tryggvason, Using statistical learning to close two-fluid multiphase flow equations for bubbly flows in vertical channels, Int. J. Multiphase Flow **85**, 336 (2016).

[10] J.-L. Wu, H. Xiao, and E. Paterson, Physics-informed machine learning approach for augmenting turbulence models: A comprehensive framework, Phys. Rev. Fluids **3**, 074602 (2018).

[11] J. Zhuang, D. Kochkov, Y. Bar-Sinai, M. P. Brenner, and S. Hoyer, Learned discretizations for passive scalar advection in a 2-D turbulent flow, Phys. Rev. Fluids **6**, 064605 (2021).

[12] K. Stengel, A. Glaws, D. Hettinger, and R. N. King, Adversarial super-resolution of climatological wind and solar data, Proc. Nat. Acad. Sci. USA **117**, 16805 (2020).

[13] G. Novati, H. L. de Laroussilhe, and P. Koumoutsakos, Automating turbulence modelling by multi-agent reinforcement learning, Nat. Mach. Intell. **3**, 87 (2021).

[14] S. Brunton, B. Noack, and P. Koumoutsakos, Machine learning for fluid mechanics, Ann. Rev. Fluid Mech. **52**, 477 (2020).

[15] F. Takens, Detecting strange attractors in turbulence, in *Dynamical Systems and Turbulence, Warwick 1980* (Springer, Berlin, Heidelberg, 1981), pp. 366-381.

[16] S. H. Bryngelson, A. Charalampopoulos, T. P. Sapsis, and T. Colonius, A Gaussian moment method and its augmentation via LSTM recurrent neural networks for the statistics of cavitating bubble populations, Int. J. Multiphase Flow **127**, 103262 (2020).

[17] Z. Y. Wan and T. P. Sapsis, Machine learning the kinematics of spherical particles in fluid flows, J. Fluid Mech. **857**, 1 (2018).

[18] P. R. Vlachas, W. Byeon, Z. Y. Wan, T. P. Sapsis, and P. Koumoutsakos, Data-driven forecasting of high-dimensional chaotic systems with long-short term memory networks, Proc. R. Soc. A **474**, 20170844 (2018).

[19] P. R. Vlachas, J. Pathak, B. R. Hunt, T. P. Sapsis, M. Girvan, E. Ott, and P. Koumoutsakos, Backpropagation algorithms and reservoir computing in recurrent neural networks for the forecasting of complex spatiotemporal dynamics, Neural Networks **126**, 191 (2020).

[20] Z. Y. Wan, P. R. Vlachas, P. Koumoutsakos, and T. P. Sapsis, Data-assisted reduced-order modeling of extreme events in complex dynamical systems, PLoS One **13**, e0197704 (2018).

[21] F. Porté-Agel, C. Meneveau, and M. Parlange, A scale-dependent dynamic model for large-eddy simulation: Application to a neutral atmospheric boundary layer, J. Fluid Mech. **415**, 261 (2000).

[22] P. E. Hamlington and W. J. Dahm, Reynolds stress closure including nonlocal and nonequilibrium effects in turbulent flows, in *39th AIAA Fluid Dynamics Conference* (American Institute of Aeronautics and Astronautics Inc., 2009).

[23] M. Samiee, A. Akhavan-Safaei, and M. Zayernouri, A fractional subgrid-scale model for turbulent flows: Theoretical formulation and a priori study, Phys. Fluids **32**, 055102 (2020).

[24] T. Chen and H. Chen, Approximations of continuous functionals by neural networks with application to dynamic systems, IEEE Trans. Neural Networks **4**, 910 (1993).

[25] T. Chen and H. Chen, Universal approximation to nonlinear operators by neural networks with arbitrary activation functions and its application to dynamical systems, IEEE Trans. Neural Networks **6**, 911 (1995).

[26] A. Akhavan-Safaei, M. Samiee, and M. Zayernouri, Data-driven fractional subgrid-scale modeling for scalar turbulence: A nonlocal LES approach, J. Comput. Phys. **446**, 110571 (2021).

[27] X.-H. Zhou, J. Han, and H. Xiao, Learning nonlocal constitutive models with neural networks, Comput. Methods Appl. Mech. Eng. **384**, 113927 (2021).

[28] X.-H. Zhou, J. Han, and H. Xiao, Frame-independent vector-cloud neural network for nonlocal constitutive modeling on arbitrary grids, Comput. Methods Appl. Mech. Eng. **388**, 114211 (2022).

[29] M. Raissi, P. Perdikaris, and G. E. Karniadakis, Physics-informed neural networks: A deep learning framework for solving forward and inverse problems involving nonlinear partial differential equations, J. Comput. Phys. **378**, 686 (2019).

[30] M. Raissi, A. Yazdani, and G. E. Karniadakis, Hidden fluid mechanics: Learning velocity and pressure fields from flow visualizations, Science **367**, 1026 (2020).

[31] M. Raissi, Z. Wang, M. S. Triantafyllou, and G. E. Karniadakis, Deep learning of vortex-induced vibrations, J. Fluid Mech. **861**, 119 (2019).

[32] J. Ling, R. Jones, and J. Templeton, Machine learning strategies for systems with invariance properties, J. Comput. Phys. **318**, 22 (2016).

[33] J. Ling, A. Kurzawski, and J. Templeton, Reynolds averaged turbulence modelling using deep neural networks with embedded invariance, J. Fluid Mech. **807**, 155 (2016).

[34] A. J. Majda, Statistical energy conservation principle for inhomogeneous turbulent dynamical systems, Proc. Natl. Acad. Sci. **112**, 8937 (2015).

[35] T. P. Sapsis, Attractor local dimensionality, nonlinear energy transfers, and finite-time instabilities in unstable dynamical systems with applications to 2D fluid flows, Proc. R. Soc. A **469**, 20120550 (2013).

[36] T. P. Sapsis and A. J. Majda, A statistically accurate modified quasilinear Gaussian closure for uncertainty quantification in turbulent dynamical systems, Physica D **252**, 34 (2013).

[37] T. P. Sapsis and A. J. Majda, Statistically accurate low-order models for uncertainty quantification in turbulent dynamical systems, Proc. Natl. Acad. Sci. USA **110**, 13705 (2013).

[38] S. Bai, J. Z. Kolter, and V. Koltun, An empirical evaluation of generic convolutional and recurrent networks for sequence modeling, arXiv:1803.01271.

[39] G. Haller and T. Sapsis, Where do inertial particles go in fluid flows? Phys. D: Nonlinear Phenom. **237**, 573 (2008).

[40] G. Haller and T. Sapsis, Localized instability and attraction along invariant manifolds, SIAM J. Appl. Dyn. Syst. **9**, 611 (2010).

[41] S. Hochreiter and J. Schmidhuber, Long short-term memory, Neural Comput. **9**, 1735 (1997).

[42] Y. Bengio, P. Simard, and P. Frasconi, Learning long-term dependencies with gradient descent is difficult, IEEE Trans. Neural Networks **5**, 157 (1994).

[43] A. Graves, A.-R. Mohamed, and G. Hinton, Speech recognition with deep recurrent neural networks, in *2013 IEEE International Conference on Acoustics, Speech and Signal Processing* (IEEE, Manhattan, New York, 2013), pp. 6645–6649.

[44] S. Shalev-Shwartz and S. Ben-David, *Understanding Machine Learning: From Theory to Algorithms* (Cambridge University Press, Cambridge, UK, 2014).

[45] A. Venkatraman, M. Hebert, and J. A. Bagnell, *Improving multi-step prediction of learned time series models*, in *Twenty-Ninth AAAI Conference on Artificial Intelligence* (AAAI, Palo Alto, California, 2015).

[46] G. Boffetta and S. Musacchio, Evidence for the double cascade scenario in two-dimensional turbulence, Phys. Rev. E **82**, 016307 (2010).

[47] V. Borue, Spectral Exponents of Enstrophy Cascade in Stationary Two-Dimensional Homogeneous Turbulence, Phys. Rev. Lett. **71**, 3967 (1993).

[48] A. Bracco and J. C. McWilliams, Reynolds-number dependency in homogeneous, stationary two-dimensional turbulence, J. Fluid Mech. **646**, 517 (2010).

[49] A. Mazzino, P. Muratore-Ginanneschi, and S. Musacchio, Scaling Properties of the Two-Dimensional Randomly Stirred Navier-Stokes Equation, Phys. Rev. Lett. **99**, 144502 (2007).